Multi-wavelet Analysis of Three-Component Seismic Arrays: Application to Measure Effective Anisotropy at Piñon Flats, California

by Lorie K. Bear,* Gary L. Pavlis, and Götz H. R. Bokelmann

Abstract We develop and apply a new technique to determine array-averaged particle motions from three-component seismic array data. The method is based on multi-wavelets, which are an extension of multi-taper spectral methods, and is a hybrid of Fourier and time-domain methods of array processing. Particle motions are determined by a time-domain principal-component method. A complex singular value decomposition is used on wavelet transformed signals assembled into multiple matrices (one for each wavelet). The eigenvector of the largest singular value of each matrix is used to estimate the phase between individual signals. We determine the relative phase between components to estimate an average particle motion ellipse for the array. The estimation procedure is made more stable by the redundancy inherent in the multi-wavelets and by M-estimators applied to individual phase factors in the complex plane. The method is applied to data from three-component array experiments conducted at Piñon Flats, California, in 1990 and 1991. We find remarkable departures of *P*-wave particle motions from the pure longitudinal motion expected for an isotropic media. Anomalies as large as 40° are measured from some azimuths. The azimuthally varying particle-motion anomalies are frequency dependent, generally increasing in magnitude as frequency increases. Borehole measurements from sensors at 153 and 274 m depth below the array show a pattern indistinguishable from the surface sensors. The data are fit with a dipping, transversely isotropic medium with a symmetry plane having a strike of 70° and a dip of 30° to the northwest. We attribute our results to three superimposed effects: (1) an anisotropy of the near surface induced by preferential weathering of the granodiorite bedrock along joints, (2) a larger scale anisotropy induced by structural and intrinsic anisotropy related to the Santa Rosa mylonite, and (3) near-surface scattering.

Introduction

In the past 8 years, a wide range of experiments have been fielded using arrays of three-component seismic stations. These arrays span apertures from 0.1 to 1000 km and provide new data on wave propagation by sampling the three-dimensional wave field at many length scales. This article focuses on quantifying the relationship of particle motions and phase velocities (slowness vectors)—a unique capability of a three-component array. This article has two distinct contributions. First, the methodology for three-component array analysis that we introduce here is new and utilizes some fundamentally different approaches from previous work. Second, the observations we make in applying this new methodology are remarkable. We find strong evidence for large departures of *P*-wave particle motions from those

predicted for a stratified, isotropic Earth—the prevailing theoretical model of the Earth in seismology.

The first part of this article introduces a new processing method for three-component arrays that simultaneously estimates three features of the incident wave field: (1) best-fitting particle motion ellipses for each station, (2) an average particle motion ellipse for the entire array, and (3) the slowness vector for a best-fitting plane wave traveling across the array. This method incorporates aspects of time- and frequency-domain beamforming (e.g., Pavlis and Mahdi, 1996; Kvaerna and Doornbos, 1986), and principal-component analysis (Vidale, 1986). The principal-component analysis is applied to all the station and component data simultaneously, much like the multi-channel detector described in Wagner and Owens (1996). Our analysis is performed on data that has been multi-wavelet transformed (similar to a windowed Fourier transform) so that the anal-

*Present address: Exxon Production Research, P.O. Box 21879, Houston, Texas.

ysis reflects the signal's behavior in a particular time window and frequency band.

The methodology developed in this article is closely related to that described in a companion article (Bear and Pavlis, 1999, this issue), and we will lean on some of the theoretical development contained therein. Both of these methodologies are dependent on the robust measurement of relative phase: either from station to station or between components of a single station. The companion article uses the robust phase measurement between stations to determine static time residuals such as would be used for seismic tomography. Here, we instead use the phase measurements between components to determine particle motion ellipses.

The most extensive recent work on three-component seismic array methodology can be found in a comprehensive suite of articles by Wagner and Owens (Wagner, 1994, 1997; Wagner and Owens, 1993, 1995, 1996). Our work, in many respects, leans heavily on these previous articles, but our approach differs in two main ways. First, our approach utilizes a recent innovation we will refer to as the multi-wavelet transform (Lilly and Park, 1995). Wagner and Owen's work focuses primarily on Fourier methods. The multi-wavelets provide a hybrid between conventional time and Fourier domain array processing methods that we will argue have some significant advantages. Second, Wagner and Owen's articles focus on so-called high-resolution methods. We experimented with high-resolution methods (Bear and Pavlis, 1997b) but found utilizing them in combination with the multi-wavelet transform led to serious stability problems. Instead of trying to maximize resolution, our approach focuses on robustness that we achieve through redundancy inherent in the multi-wavelets and the inherent redundancy of array data. We would argue this is an important strength of this methodology over other approaches that have been applied to this problem.

On the observational side, the closest previous work to this article was that done by Bokelmann (1995a, 1996). Bokelmann used data from GERESS, an array in southern Germany composed of 25 single-component stations. Five of these stations have co-located three-component sensors. Bokelmann determined the slowness vector by processing the vertical-component array data. He then used conventional particle motion analysis methods applied to each of the five three-component stations at GERESS and averaged the results. Our results differ in that all the data we examine are from full three-component seismic arrays. As a result, we determine a best slowness vector and best-fitting particle motion ellipse simultaneously from all the available data. In addition, the methodology developed here can be applied in multiple frequency bands to examine the frequency dependence of particle motion relative to a measured phase velocity. On the other hand, our results can be directly related to Bokelmann's (1995a) as we apply the same inversion procedure below to determine an anisotropic model to fit our observational data.

Method

The approach we use here is closely related to ideas described in a companion article by Bear and Pavlis (1999). Some background is found in that article that will not be repeated here for the sake of brevity. The primary difference is in how we exploit the relative phase between a group of signals. Consider a pure harmonic signal at frequency f. In this simple situation, the phase differences between stations m and n can be considered equivalent to a time difference between the two signals through the relation

$$e^{i(\theta_m - \theta_n)} = e^{i2\pi f(t_m - t_n)}. \tag{1}$$

This relation was used in Bear and Pavlis (1999) to determine time residuals. On the other hand, the vector formed from the three components of a given station for a pure harmonic signal

$$[r_1 e^{i(2\pi ft + \phi_1)}, \quad r_2 e^{i(2\pi ft + \phi_2)}, \quad r_3 e^{i(2\pi ft + \phi_3)}] \tag{2}$$

defines an ellipse of instantaneous particle motion in three dimensions. The details of the ellipse are determined by the magnitude and relative phase of the three different components. It is this relation that is most applicable to the problem at hand. The key point is that with signals that are localized in frequency, the relative phase is the key quantity to be measured.

For an array of N three-component stations and K time samples, we start by creating the $3N \times K$ complex data matrix $\mathbf{A}(f, t, \mathbf{p})$, which can be partitioned into three $N \times K$ matrices:

$$\mathbf{A}(f, t, \mathbf{p}) = \begin{bmatrix} \mathbf{A}^x(f, t, \mathbf{p}) \\ \mathbf{A}^y(f, t, \mathbf{p}) \\ \mathbf{A}^z(f, t, \mathbf{p}) \end{bmatrix},$$

where

$$A_{nk}^c(f, t, \mathbf{p}) = \mathcal{W}[s_n^c][f, t_k + \tau(\mathbf{p}, n)]. \tag{3}$$

$\mathcal{W}$ denotes an integral transform for studying the signal behavior near frequency f, s_n^c is the data recorded on the cth component of the nth station, and the $\tau(\mathbf{p}, n)$ are time shifts to account for travel-time differences between stations due to a plane-wave arrival with slowness vector $\mathbf{p}$, or due to some more complex travel-time function [e.g., τ may contain a static correction relative to a plane-wave model determined as described in Bear and Pavlis (1999)]. The integral transform we choose to use is the multi-wavelet transform developed by Lilly and Park (1995). We make this choice largely because of an important advantage it inherently has in applications to modern broadband data: the multi-wavelet functions are "wavelets" in the sense that their timescales can be adjusted to match the frequency scale being resolved.

That is, wavelets for lower frequency bands are naturally longer in time than those for higher frequency bands.

The rows of **A** consist of K samples of the wavelet transformed data, each over a slightly different time window. If we assume that the signal of interest propagates with a constant slowness vector over the times involved, then each column of **A** provides the same information on the signal plus the effect of noise. We use times $t_k = [t + (k - 1)\Delta t]$, $k = 1, \ldots, K$, where Δt is chosen so that $t_K - t_1$ is the length of one-half to one cycle of the center frequency f. This choice is not unique, but we have found it useful for reducing the computational load of this procedure.

The complex matrix **A** can be written as a singular value decomposition

$$A = U \Lambda V^\dagger, \quad (4)$$

where **U** and **V** are unitary matrices and Λ is a real diagonal matrix. We assume the SVD is organized such that $\lambda_1 \geq \lambda_2 \ldots \geq \lambda_{\min(N,K)}$. **U** can be considered a rotation of the data such that the column

$$\mathbf{u}_1(f, t, \mathbf{p}) = \begin{bmatrix} u_1^x(f, t, \mathbf{p}) \\ u_1^y(f, t, \mathbf{p}) \\ u_1^z(f, t, \mathbf{p}) \end{bmatrix} \quad (5)$$

points in the direction of largest energy. We then perform the beamforming process by searching through possible slowness vectors **p**. We choose the best slowness vector by maximizing the coherence measure

$$S(f, t, \mathbf{p}) = \max_{c=x,y,z} \frac{\|\lambda_1(f, t, \mathbf{p})\mathbf{d} \cdot \mathbf{u}_1^c(f, t, \mathbf{p})\|^2}{\|\mathbf{d}\|^2 \|\lambda_1(f, t, \mathbf{p}) \mathbf{u}_1^c(f, t, \mathbf{p})\|^2}, \quad (6)$$

where $d_n = 1/N$ for $n = 1, \ldots, N$. This measure is analogous to semblance (Husebye and Ruud, 1989) in that the denominator measures the average of the station powers and the numerator measures the power of the stack.

The matrix **A** can also be partitioned by stations such that

$$\mathbf{A}(f, t, \mathbf{p}) = \begin{bmatrix} \mathbf{A}^1(f, t, \mathbf{p}) \\ \vdots & \vdots \\ \mathbf{A}^N(f, t, \mathbf{p}) \end{bmatrix},$$

where

$$A_{ck}^n(f, t, \mathbf{p}) = \mathcal{W}[s_n^c][f, t_k + \tau(\mathbf{p}, n)]. \quad (7)$$

Each of the partition matrices can be considered as a portion of a 3 × 3 covariance matrix

$$\mathbf{R}(f, t, \mathbf{p}) = \frac{1}{K} \mathbf{A}^n(f, t, \mathbf{p}) \cdot \mathbf{A}^{n\dagger}(f, t, \mathbf{p}). \quad (8)$$

We showed in Bear and Pavlis (1997a) that the real and imaginary parts of the multi-wavelet transforms behave as the analytic filtered signal. Thus **R**$(f, t, \mathbf{p})$ is analogous to the 3 × 3 covariance matrix used by Vidale (1986) for principal-component analysis of the signal's particle motion. We have already determined the N principal components in

$$\mathbf{u}_1(f, t, \mathbf{p}) = \begin{bmatrix} \mathbf{u}_1^1(f, t, \mathbf{p}) \\ \vdots \\ \mathbf{u}_1^N(f, t, \mathbf{p}) \end{bmatrix} \quad (9)$$

so that the complex values in the eigenvector associated with the largest singular value, $\mathbf{u}_1^n$, describe the particle motion for the signal at station n over the time and frequency windows used.

The use of the multi-wavelet transform is particularly appropriate here, since we are interested in a phenomenon that is expected to vary significantly both in time and in frequency. The real and imaginary parts of the kernels to the multi-wavelet transforms are specifically designed as real, discrete, finite time series that have their energy concentrated within a frequency band defined by the center frequency f and a bandwidth $2f_w$, where $f_w \leq f$ (Lilly and Park, 1995; Bear and Pavlis, 1997a). The form of the multi-wavelets we used here can be found in Figure 1 of the companion article by Bear and Pavlis (1999). The multi-wavelet functions occur in even and odd pairs, where each pair emphasizes a different portion of the time and frequency windows. The lengths of the time and frequency windows determine how many transforms can be used (Lilly and Park, 1995). In this study, we produced five usable transforms for each fre-
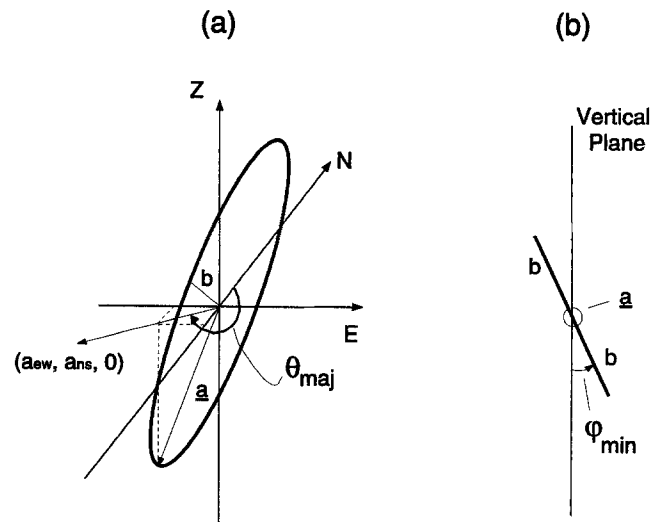
(a)   **(b)**

Figure 1. Picture of an ellipse in (a) three-dimensional view and (b) a view where the major axis **a** is pointing out of the page. By convention, $\phi_{\min}$ is positive when the minor axis is rotated clockwise and negative when rotated counter-clockwise. In this case, $\theta_{\maj}$ would be approximately 240°, and $\phi_{\min}$ would be approximately $-25°$.

quency band following Bear and Pavlis (1997a). We emphasize, however, that this choice is not unique. Longer analysis windows and/or different frequency bandwidths could be used to define different wavelets with a differing number of usable functions.

It is important to emphasize that our method is a multichannel procedure. It determines estimates of elliptical particle motions for each of the N stations in the context of producing the most coherent beam for all three components of the entire array. It is also important to remember that we have N ellipse estimates over a small spatial area for each of the five multi-wavelet transforms. This means that we can parlay this redundancy into more stable results for each station (by using the five pieces of data from the different transforms) and for the array as a whole (by using the $5N$ pieces of data from all the stations and the different transforms). Note, however, that the absolute phase estimates determined using different multi-wavelet functions cannot be compared directly, due to the relative phase differences between the complex wavelets that we have found no way to unambiguously resolve.

An ellipse can be completely described by the spatial orientations and lengths of the major and minor axes. We characterize the particle motion by three main observables (Fig. 1). First, there is the linearity of particle motion for station n. We use a standard measure called rectilinearity defined as $e_n = 1 - b_n/a_n$, where $2a_n$ and $2b_n$ are the major and minor axes lengths, respectively. Second, we measure the azimuth of the projection of the major axis onto the horizontal plane that we will refer to with the symbol $\theta_{maj,n}$. Finally, we compute the angle between the minor axis and the vertical plane $\phi_{min,n}$ when looking down the major axis. For P waves propagating in a homogeneous, isotropic, horizontally layered medium, the ellipticity in the particle motion will be induced mainly by P-to-S conversions at the layer contacts. Thus, the elliptical motion should be contained in the radial-vertical plane such that $\theta_{maj,n}$ should be the same as the propagation azimuth (determined from the slowness vector) and $\phi_{min,n}$ should be zero. We will refer the deviation of the major axis projection angle from the propagation azimuth ($\theta_{maj,n} - \theta_p$) as the major axis skew, and the angle between the minor axis and the vertical plane $\phi_{min,n}$ as the minor axis tilt.

We need similar values to describe the average elliptical particle motion for the entire array. There are multiple ways that one could average the results obtained for each station from the individual multi-wavelet transforms. We chose a dual averaging scheme that is made robust by using an M-estimator (Bear and Pavlis, 1997a; Chave et al., 1987). The M-estimator is used at each averaging step because it removes the effects of any outlying values. For the rectilinearity e, we average over the e_n determined from each multi-wavelet transform separately and then average the values for the five multi-wavelet transforms to obtain the final value. We determine an average array major axis by first averaging all the station major axes determined using a given

multi-wavelet transform. This leaves us with five samples of the array major axis orientation—one for each transform. In this article, we are primarily interested in determining the azimuth of the projection of the major axis onto the horizontal plane. To compute this angle, we normalize the lengths of the five major axis samples to one and perform another average to determine the array major axis. We then compute θ_{maj}, which is the azimuth of the projection of the array major axis onto the horizontal plane. A similar process is applied to determine the array minor axis. The only difference is that the station minor axes are all projected onto the plane perpendicular to the array major axis. This assures that the array minor axis is perpendicular to the array major axis as is necessary for an ellipse.

Piñon Flat

Numerous seismic arrays have been deployed at Piñon Flat because of its characterization as a hard-rock site (e.g., Vernon et al., 1991; Al-Shukri et al., 1992; Owens et al., 1991). Piñon Flat is a nearly planar erosional surface in the San Jacinto Mountains, California, located 12 km northeast of the San Jacinto fault system and 25 km southwest of the San Andreas fault system (Fig. 2). It has approximately 60 m of weathered material floored by plutonic rocks of granodiorite composition (Wyatt, 1982; Fletcher et al., 1990).

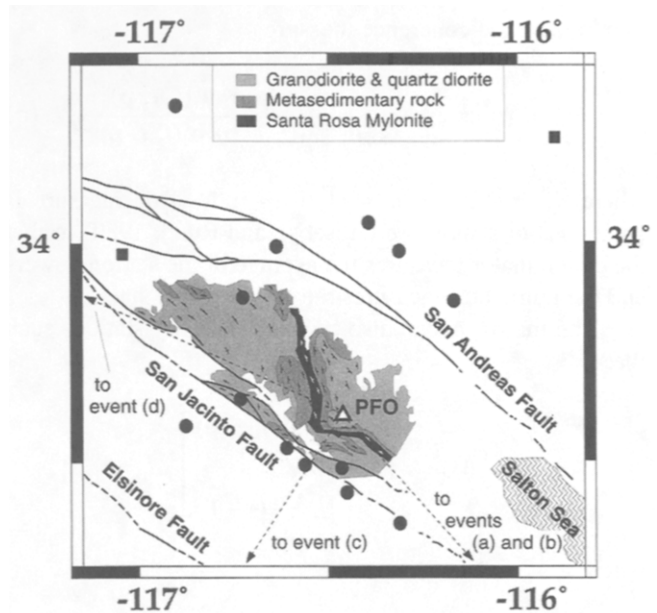We analyzed local event data from two seismic arrays

Figure 2.   Map of area surrounding Piñon Flat. The geology is modified from Dibblee (1981). The locations for the events recorded by PFO-HF are plotted as filled circles, and those recorded by PFO-BB are plotted as filled squares. Events (a), (b), and (d) were recorded by PFO-HF and have θ_{loc} values of 139° (1), 139° (2), and 296°, respectively. Event (c) was recorded by PFO-BB and has $\theta_{loc} = 213°$.

at Piñon Flat—a very small aperture high-frequency array (PFO-HF) and a larger aperture broadband array (PFO-BB). We focused on studying local events due to some intriguing observations that had been made earlier with data recorded with the PFO-HF array. Vernon *et al.* (1998) plotted the raw station particle displacements for the first *P* arrival in a three-dimensional display for one of the same events we analyzed here. They note that (1) the motions are strongly elliptical and (2) the major axes of the motions are skewed from the great circle path backazimuth.

The PFO-HF array consists of two borehole sensors and 58 surface sensors (Fig. 3). All stations were equipped with 2-Hz, three-component seismometers. The nominal sensor spacing is 7 m in the grid and 21 m along the arms (Owens *et al.*, 1991). This array operated between 18 April and 27 May 1990 and recorded triggered data at 250 samples/sec. We studied 16 events from PFO-HF, chosen for their coverage of arrival azimuths, signal-to-noise ratio, and data recovery. The event locations are plotted as filled circles in Figure 2, and source parameters are listed in Table 1. Note that no events were recorded by this array in a 90° gap to the east of the array.

We applied the processing described in the Method section to the surface sensors in the frequency bands 7 to 21 Hz (time length 0.428 sec) and 2 to 6 Hz (time length 1.5 sec). These bands were chosen to coincide with the change in signal behavior noted by both Vernon *et al.* (1998) and Wilson (1997) at approximately 8 Hz. The vertical-component beams [determined using a time-domain beamforming program called dbap (Harvey, 1994)] for these 16 events are plotted in Figure 4. This figure also shows the window over which the transforms were applied for the processing. The windows were chosen automatically by an algorithm that searched for the maximum coherence (equation 6). For most events, this window only overlaps with the first few cycles of the *P* wave, but for more emergent events, it sometimes is chosen at a later time. For this figure and the discussion that follows, we define three different angles: θ_{loc} is the backazimuth predicted by a great circle path from the source to the receiver, θ_p is the backazimuth measured by slowness analysis from the array, and θ_{maj} is the backazimuth measured from the average *P*-wave particle motion major axis.

We also independently processed data from the two borehole sensors in the 7- to 21-Hz frequency band. We determined estimates for the best-fit particle motion ellipses treating these data as a two-station array with a fixed slowness vector equal to that determined by the surface array for each event. Due to data problems, we did not process the events with $\theta_{loc} = 43°$, $177°$, $296°$, and $321°$ for the borehole sensors.

We were not able to analyze data from the PFO-HF array in frequency bands lower than 2.0 Hz due to its small aperture and to its use of high-frequency sensors. The larger aperture of the PFO-BB array and the use of broadband sensors allowed us to study the wave-field behavior in a lower frequency band of 0.75 to 2.25 Hz (time length 4.0 sec).
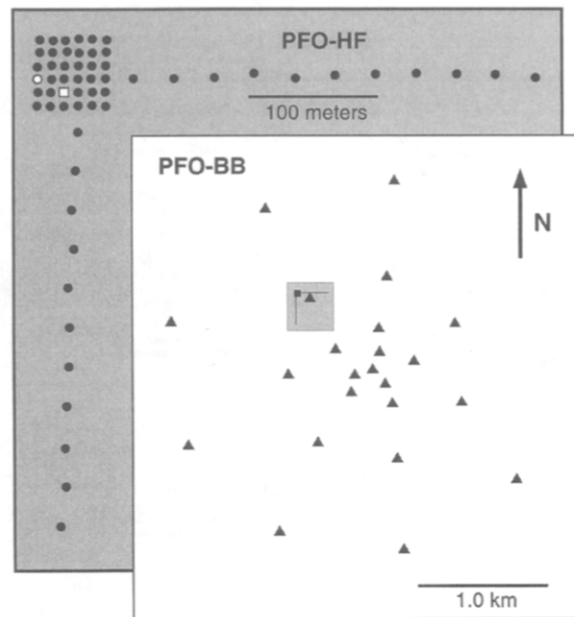

Figure 3. Station locations for the two arrays at Piñon Flat. All the symbols in the shaded region denote positions of surface sensors for PFO-HF. The open symbols also denote the approximate positions of the borehole sensors. The borehole sensor at the open circle is at 153 m depth, while the borehole sensor at the open square is at 274 m depth. The stations of PFO-BB are shown in the unshaded region as filled triangles. The relative position and scale of PFO-HF to PFO-BB is shown schematically in the unshaded region.

Table 1
Information about the Events Plotted in Figure 2

| θ_{loc}	Date/Time	Array	#sta	Δ (degrees)	Depth (km)	m_l
7	1990117:12:52:42	PFO-HF	51	0.44	0.0	2.3
18	1990132:23:54:47	PFO-HF	55	0.39	4.8	2.5
43	1990109:20:24:58	PFO-HF	51	0.36	4.2	2.4
139(1)	1990137:17:02:50	PFO-HF	53	0.99	6.9	3.3
139(2)	1990137:19:32:50	PFO-HF	53	0.99	7.0	3.4
153	1990139:09:48:20	PFO-HF	53	0.27	12.5	2.1
177	1990136:01:14:16	PFO-HF	57	0.17	11.1	2.4
181	1990122:11:34:57	PFO-HF	53	0.12	7.0	2.1
217	1990132:19:42.47	PFO-HF	50	0.14	9.7	1.4
239	1990134:05:05:21	PFO-HF	57	0.14	11.8	2.6
266	1990138:12:05:43	PFO-HF	51	0.35	13.3	1.7
280	1990130:07:23:31	PFO-HF	57	0.23	15.7	2.1
296	1990110:03:24:59	PFO-HF	51	1.16	3.5	3.6
321	1990137:18:44:27	PFO-HF	53	0.35	17.3	1.4
333	1990124:02:23:22	PFO-HF	55	0.79	10.2	2.6
339	1990139:06:30:58	PFO-HF	53	0.41	5.0	2.7
36	1991057:17:08:30	PFO-BB	20	0.78	1.6	2.7
213	1991088:04:55:20	PFO-BB	23	1.80	6.0	3.0
308	1991077:03:58:26	PFO-BB	20	0.61	11.7	2.6
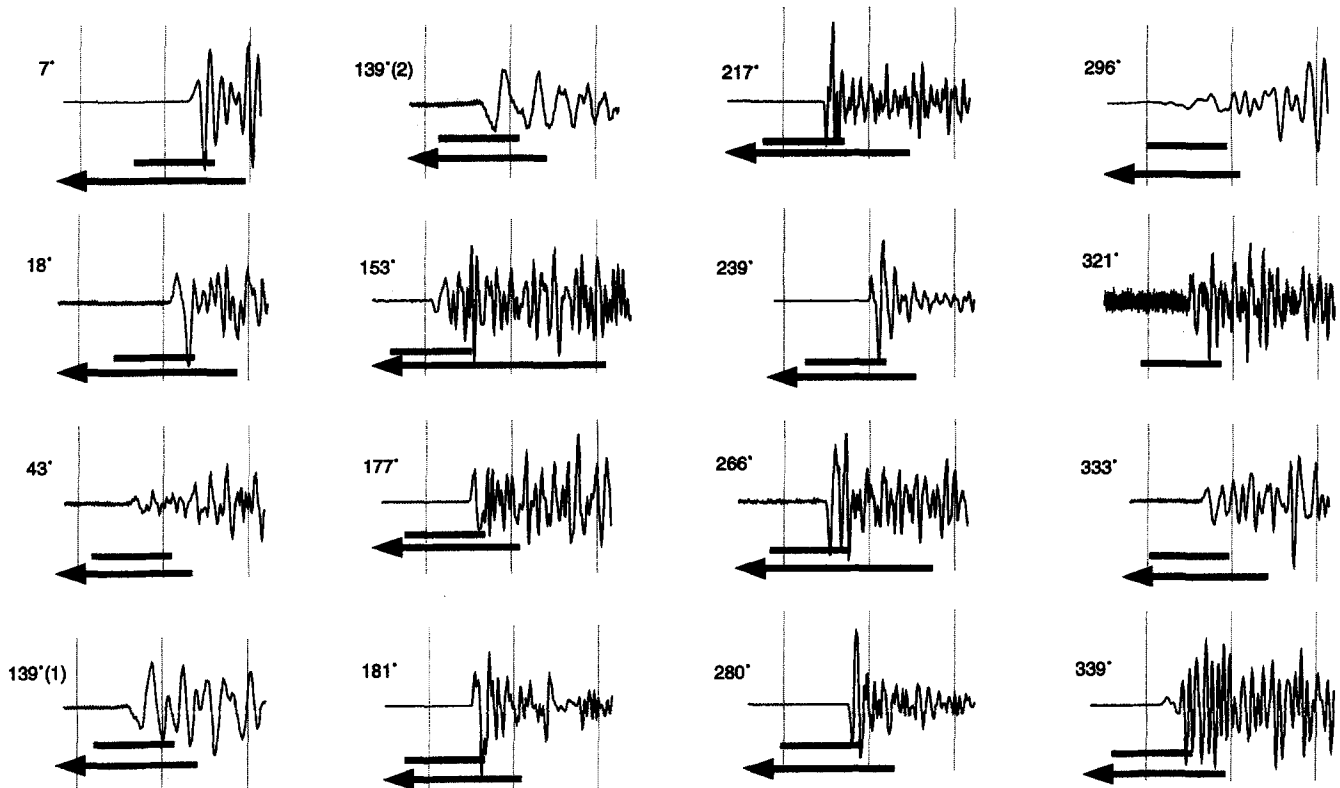
Figure 4.   Vertical-component beams for events recorded by PFO-HF normalized to peak amplitude. The labels refer to each event's θ_{loc}, and the thin vertical lines denote 0.5-sec marks. The placement of the multi-wavelet transforms are shown as thick horizontal lines. The entire time window is shown for the 7- to 21-Hz transforms. The arrowheads specify that the remainder of the time windows for the 2- to 6-Hz transforms are earlier in time. Note that the time windows generally overlap with the signal for no more than three cycles of the transform's center frequency.

This array consisted of 28 three-component broadband Streckeisen STS-2 sensors arranged in five concentric circles named A through E (Al-Shukri *et al.*, 1992). The three sensors of the outer E-ring had a large influence over the beam pattern of this array, and the loss of any particular station caused severe distortions in the beam pattern. Because two different E-ring stations were down for two of the three events we studied from this array, we decided not to use any of the data from the outer E-ring. We also had to throw out two of the D-ring stations due to data problems. Thus, we ended up with the 23 stations shown in Figure 3. This reduced array had an effective aperture of 3 km. We present results for three events whose locations are shown as filled squares in Figure 2. Detailed source parameters are listed in Table 1. Unfortunately, these were the only local events that had good enough signal-to-noise ratios for processing in the frequency band of interest (0.75 to 2.25 Hz).

Observations

In Figure 5, we plot the array major axis skew ($\theta_{maj} - \theta_p$) versus the propagation direction, θ_p, and the location skew, ($\theta_{loc} - \theta_p$), versus θ_p for the three frequency bands. The hor-

izontal and vertical lines are error bars for θ_{maj} (vertical lines in Fig. 5a) and θ_p (all other lines). The error bars for θ_{maj} were determined by first finding a sphere around the array major axis that contained at least three of the five samples determined by averaging the station major axes for each multi-wavelet transform. The range of azimuths covered by the projection of the sphere onto the horizontal plane was then used as an error estimate. A similar process was used to determine the error for θ_p from the five slowness vector samples. This is similar to the methodology for quantifying slowness vector errors described by Bear and Pavlis (1997a), but the time-averaging required in equation (7) implies that the samples used to produce these error bars are not statistically independent. Note the systematic variations in the array major axis and location skews with propagation direction.

These regular variations can also be seen in individual station results. Figure 6 shows the major axis skews for individual stations from a subset of the events we examined. (The arms of the PFO-HF array are not shown so that the grid data can be seen more clearly.) We see the data show a consistent background skew that defines the array average with a superimposed smoothly varying pattern of deviations
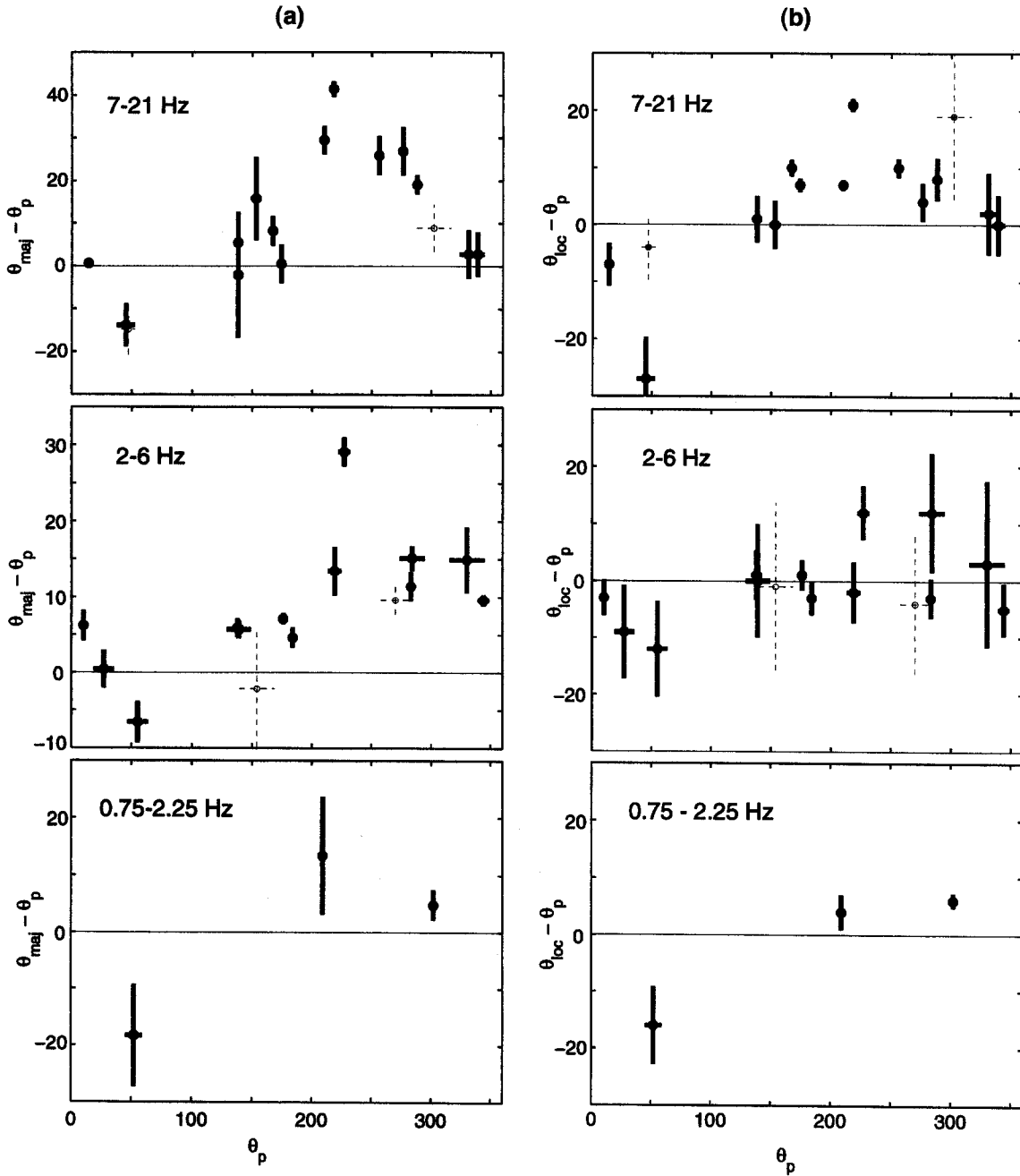
Figure 5. Plots of (a) $(\theta_{maj} - \theta_p)$ and (b) $(\theta_{loc} - \theta_p)$ versus θ_p with error bars. The open circles with dashed error bars are associated with events that have at least 20 stations with signal-to-noise ratios of 2:1 or less. Note the persistent pattern over all three frequency bands, particularly in (a).

within the array. The consistency, in fact, is even better for the PFO-HF data than it may appear at first glance. There are five stations—X0Y1, X3Y5, X3Y6, X4Y0, and X4Y2—that have consistently more negative skews than the other stations. We suspect that their behavior is due to problems with one of the three sensors of those stations. The individual station results for the PFO-BB data show a sense of skew consistent with the array average, but we do not see the smoothly varying trends that are apparent from the PFO-HF

data. This is an important observation as it indicates that there is an overall pattern that distorts particle motions for the entire PFO-BB array, but the smoothly varying patterns seen in the PFO-HF data occur at scale lengths smaller than the station spacing of the PFO-BB data.

The rectilinearity, e, for the three frequency bands is plotted in Figure 7 versus propagation azimuth θ_p. Note that the particle motion is markedly more elliptical in the 7- to 21-Hz band than in either of the other frequency bands. This
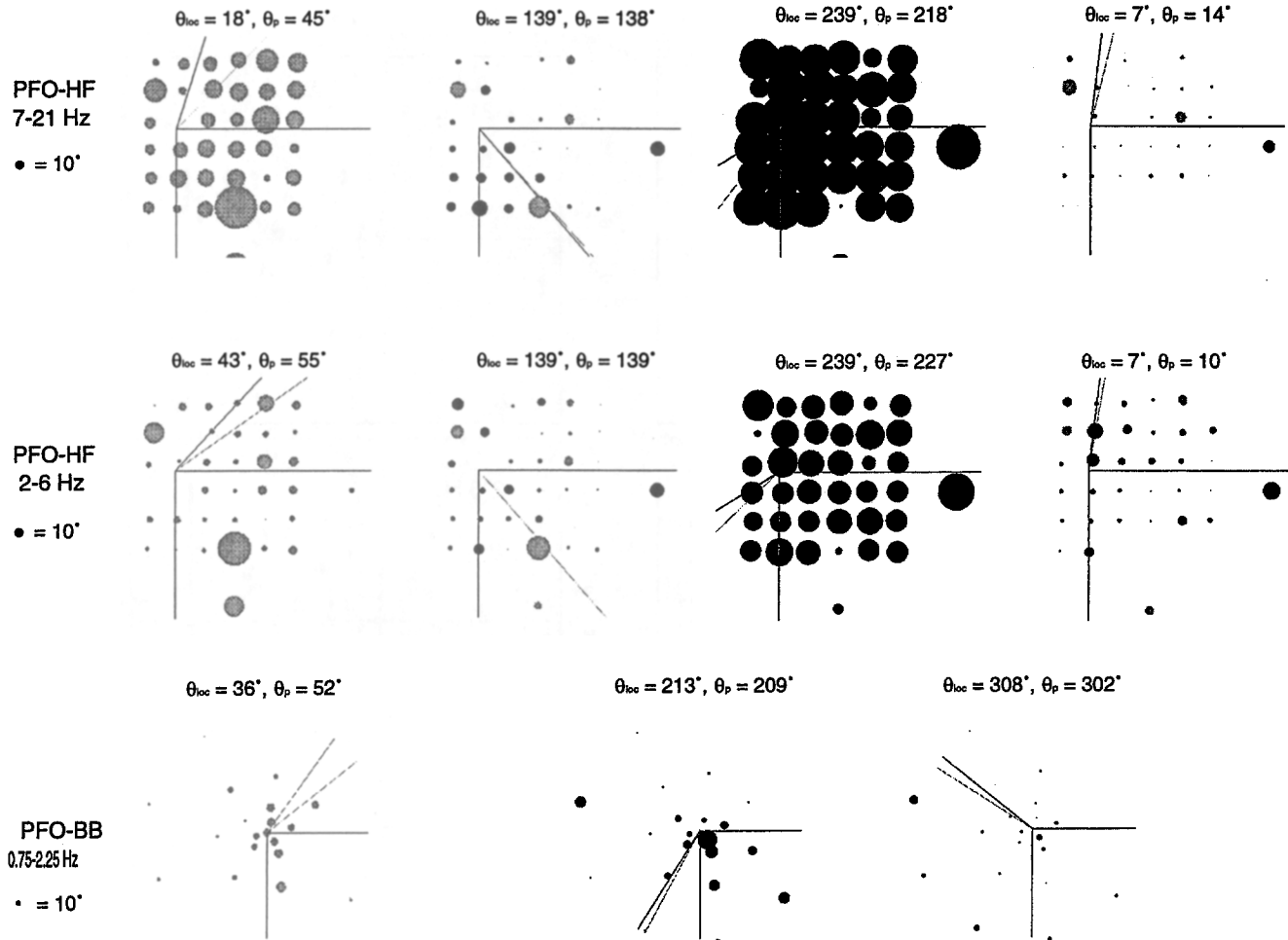
Figure 6.   The absolute magnitudes of $(\theta_{maj,n} - \theta_p)$ for the raw station data. A sphere of radius $\| (\theta_{maj,n} - \theta_p) \|$ is plotted at the position of each station in the array. A black sphere is plotted if $(\theta_{maj,n} - \theta_p)$ is positive; a gray sphere, if $(\theta_{maj,n} \theta_p)$ is negative. The scales for the radii are shown to the left. Only the grid of PFO-HF is shown due to space and resolution limitations. The axes point to the east and south, the solid lines point in the direction of θ_{loc}, and the dashed lines point in the direction of θ_p.

matches the difference in the behavior of the PFO-HF data above and below 8 Hz noted by Anderson (1993) and Vernon *et al.* (1998). In Figure 8, we plot the station minor axes tilts $(\phi_{min,n})$ for the PFO-HF data in the 7- to 21-Hz frequency band. We do not show the comparable figures for the other frequency bands because the orientations of the minor axes are not meaningful for signals that are linearly polarized. We note that there is a consistent pattern to the orientations of the minor axes across the array. This is remarkable considering there is no spatial smoothing in this processing scheme. The patterns in magnitude and sign for the minor axes orientations are very similar to those shown in Wilson and Pavlis (1999) for spectral amplitude variations.

We suggest that the elliptical particle motions of the signals in the 7- to 21-Hz band (see Fig. 7) is caused mainly by near-surface focusing and scattering effects. Further demonstration of this comes from the two borehole instruments, which are both well below the weathered layer (Fletcher *et*

al., 1990). We note that these signals are much more linearly polarized than those recorded at the surface. The rectilinearity values range from 0.8275 to 0.9894 and track well with the curve for the 2- to 6-Hz frequency band in Figure 7. On the other hand, the station major axis skews $(\phi_{maj,n} - \theta_p)$ versus θ_p do not appear to be a strictly near-surface affect. In Figure 9, we plot the polarization properties for the two borehole stations along the averaged surface sensor values from Figure 5a. The strong agreement of these results indicates a more deep-seated source for the observed skews.

Discussion

Our analysis of the data from Piñon Flat revealed five significant observations.

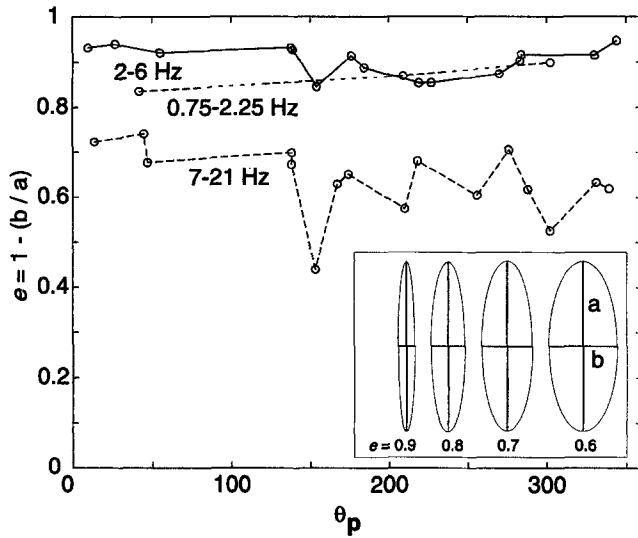1. The difference between the propagation azimuths and the

Figure 7. This figure shows the rectilinearity, e, versus the propagation azimuth θ_p for all the events in the three frequency bands.

array major axis skews have a regular pattern that is consistent in all three frequency bands (Fig. 5a).

2. The difference between the propagation azimuths measured by array analysis and the location azimuths also have a regular pattern very similar to that of the array major axis skews. This pattern holds in all three frequency bands, though it is most pronounced in the 7- to 21-Hz band (Fig. 5b).

3. The particle motions in the 2- to 6-Hz and 0.75- to 2.25-Hz frequency bands are nearly linear (Fig. 7).

4. The particle motions in the 7- to 21-Hz frequency band for the surface sensors are much more elliptical (Fig. 7). The tilts in the minor axes from the vertical plane, though, are not random. There is a very distinct pattern in magnitude and sign across the array (Fig. 8).

5. The particle motions for the borehole sensors in the 7 to 21-Hz frequency band are nearly linear, but the pattern of major axis skews is nearly indistinguishable from the surface sensors. (Fig. 9).

These observations are not what is expected for standard Earth models. Most theoretical seismology assumes the Earth is a horizontal stack of homogeneous, isotropic layers. But such a model cannot account for any of the observations listed above. Lin and Roecker (1996), using data from the PFO-BB experiment, measured differences between location and propagation azimuths for regional events analogous to the plots in Figure 5b. They modeled this behavior with a single dipping layer with moderate success. The difference between their study and this one, however, is that they did not investigate particle motion variation with respect to the propagation azimuths. They looked only at phase velocity variations from that expected from independently determined event locations. This is a significant point about our

results compared to most previous work—we are measuring *P*-wave particle motion relative to phase velocity vectors measured by the same array (e.g., observation 1). For even a complex stack of nonparallel dipping layers, conventional ray theory for isotropic media, which is based on a high-frequency limit (Aki and Richards, 1980, pp. 84–105), would predict no difference between the *P*-wave particle motion direction and the azimuth defined by the array slowness vector. This means that the values plotted in Figure 5a should be identically zero.

Because of the inadequacy of conventional layer models, we tried modeling the behavior of these data with a simple anisotropic medium. The model we use is one level of complexity above a dipping isotropic layer. That is, we treat the entire volume beneath the array as a dipping, transversely isotopic medium. Using the inversion method described by Bokelmann (1995a,b, 1996), the 7- to 21-Hz data were fit with a medium with the following properties: (1) the normal vector to the plane of symmetry dips 60° from the vertical and points 20° west of north, and (2) the medium is characterized by $\eta = 0.65$ and $\tau = 0.3$ [defined in Bokelmann (1995a)] The results are shown in relation to the data in Figure 9. (Results from inversion of the 2- to 6-Hz data were similar but are not shown for the sake of brevity.)

The transversely isotropic model yielded a variance reduction of 57% for the 7- to 21-Hz data. Although this is a significant improvement over a dipping layer model, it still has some serious inadequacies. This model fits the gross pattern of these data, but comparison to Figure 5b shows we are not completely fitting the data within our measured error bars. There are two explanations for this: (1) the error bars underestimate the real uncertainties in the particle motion major axes, or (2) the model is inadequate. Although the error estimates we obtain here have theoretical weaknesses (discussed earlier), we doubt they are drastically in error. Furthermore, the consistency of individual station particle motions (Fig. 6) argue against this. The implication is that the model we have determined is an oversimplification.

The anisotropy implied by this model is exceptionally strong. We compute that *S*-wave splitting would theoretically approach 30% in some directions for such a medium. This is much larger than reported *S*-wave splitting for the Anza region by Peacock *et al.* (1988). They observed *S*-wave splitting in this region of the order of 2% and less. We note, however, that very little of their data were from PFO. Furthermore, *S*-wave splitting measurements are based on an effect accumulated on the entire path from a source to a receiver, while what we measure is a local effect controlled primarily by the elastic properties of the earth directly under the array.

What is the source of the observed particle motion deviations we observe here, and does the anisotropic model we determined have any relationship to reality? The answer is ambiguous and points out a fundamental weakness in our existing theoretical models for wave propagation in the real Earth. That is, the earth is unquestionably a heterogenous
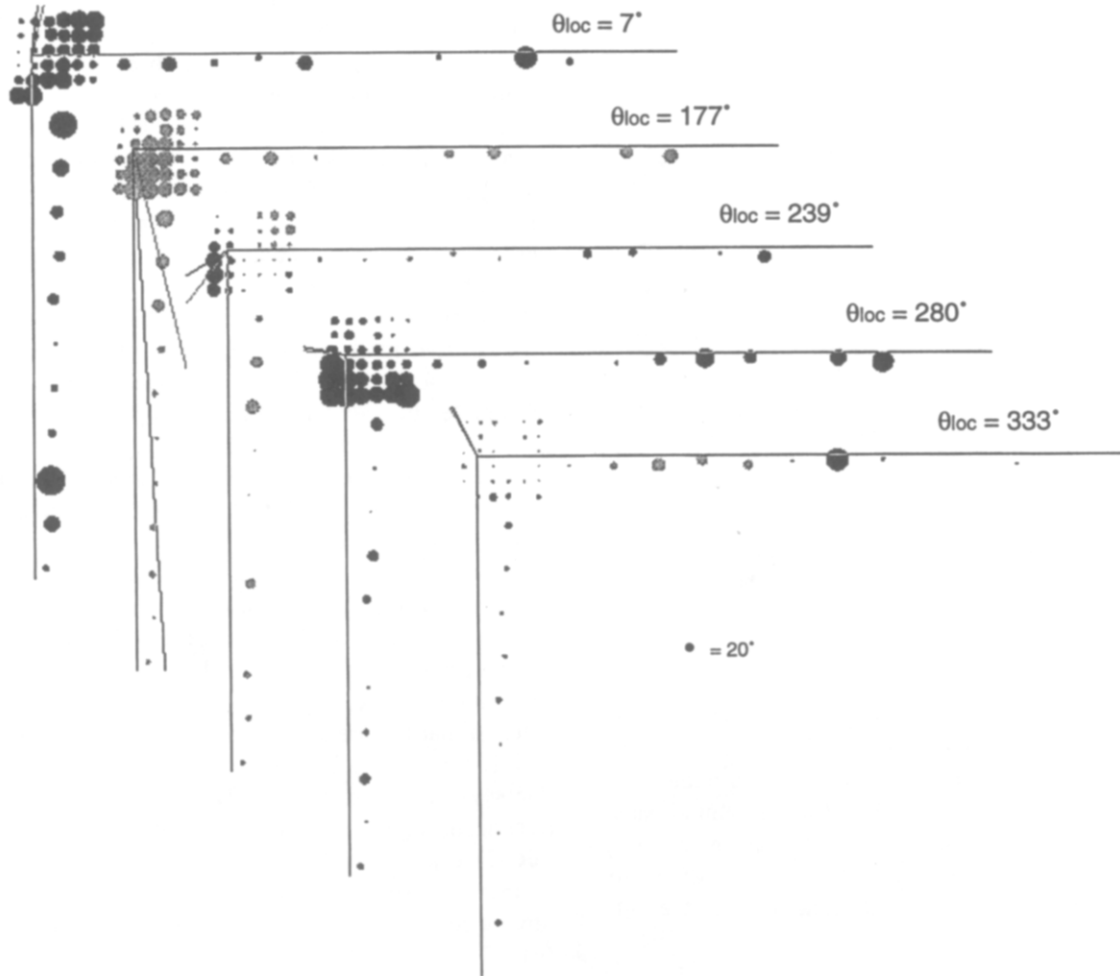
Figure 8. PFO-HF station data for $\phi_{min,n}$ in the 7- to 21-Hz frequency band for five location azimuths. A sphere of radius $\| \phi_{min,n} \|$ is plotted at the position of each station in the array. A scale is shown in the lower right corner. A black sphere is plotted if $\phi_{min,n}$ is positive; a gray sphere, if $\phi_{min,n}$ is negative (see Fig. 1 for definition of positive and negative). Note the regular patterns that exist across the array.

media with seismic properties that fluctuate over a huge range of scale lengths ranging from the grain size of a given rock (~1 mm) to thousands of kilometers. Seismic wavelengths range from the order of a few meters to thousands of kilometers. A poorly understood, fundamental problem is how inhomogeneity of a given scale is expressed observationally. We all understand that a rock with a preferred orientation of minerals like a schist is intrinsically anisotropic because the fabric that defines the anisotropy is at a scale far below the smallest observed seismic waves. Fabric at intermediate scales, however, can induce anisotropic effects that are more difficult to sort out. It has been known for more than three decades [based on landmark work by Backus (1962)] that layered sedimentary rocks are anisotropic at wavelengths that are large compared to the scale of the layering. Thus, a layered model over some range of wavelengths must pass from conventional, high-frequency limit behavior to a behavior more analogous to that of an intrinsi-

cally anisotropic material. Theoretical progress has been made toward relating anisotropic effects of different scales (see, e.g., Werner and Shapiro, 1998), but the problem remains poorly understood at best. [For a good fundamental physical understanding of this issue, the reader is referred to Chapter 1 of the book by Helbig (1994).] The issue this raises for this article is that to understand our results, we need to review what we understand about heterogeneity of the Earth within the vicinity of Piñon Flat at a range of relative scales. We organize this discussion in order of increasing scale length.

Bedrock at Piñon Flat is a granodiorite with grain sizes of the order of a few millimeters and no appreciable fabric (i.e., no intrinsic anisotropy). At the scale of 1 to 100 m, however, the situation is drastically different. The near surface at Piñon Flat is an ancient weathering profile that has altered the original granodiorite to a depth of at least 60 m (Fletcher et al., 1990). The geologic processes that created
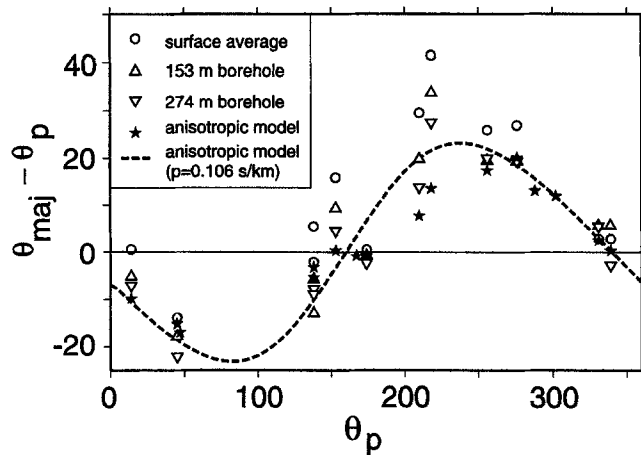
Figure 9. This figure plots deviations of the particle motion azimuths determined from *P* waves from that expected for a pure longitudinal wave (major axis skews) as a function of the measured phase velocity azimuth. Data from both the surface array average (circles) are shown here in relation to single-station particle motions measured in the two boreholes in the PFO-HF experiment (upright and inverted triangles). All measured results plotted are for the 7- to 21-Hz band. The star symbols and the dashed lines are predictions of major axis skews for the anisotropic model discussed in the text. The stars show the actual predicted value that takes into account the measured phase velocity across the array. The dashed line shows the prediction for the anisotropic model at a constant ray parameter, but varying azimuth. It illustrates the sinusoidal pattern that characterizes this dipping, transversely isotropic model.

this weathering layer are unique to granitic rocks (Ollier, 1969) and produce an extremely heterogeneous medium. Granitic rocks are weathered preferentially along preexisting joints because the primary agent of weathering is chemical attack by water. Water flow is focused on the enhanced permeability zone around a joint in the rock leading to concentrations of weathering along these surfaces. The result is largely unaltered corestones surrounded by rings of progressively more altered material. Preferred orientation of joints, which is almost universally observed, will lead to a characteristic fabric of the near surface. We suggest this may lead to an effectively anisotropic media at the higher frequencies we are observing. At these frequencies, the wavelength of the *P* waves we record are of the same order of magnitude as the entire weathered layer. We suggest this leads to bulk elastic properties of the near surface that are a major factor in producing all the particle motion deviations we observe, particularly in the upper frequency band of 7 to 21 Hz. At the same time, the large variations in properties within the weathered layer undoubtedly strongly scatter the incident wave field as argued by Vernon *et al.* (1998). At the frequencies we are working with here, the scattering and induced anisotropy could well be thought of as essentially

the same phenomenon—distortion of observed ground motion induced by near-surface heterogeneity.

The weathered layer, however, is probably not the whole story. It does not fully explain the borehole data, and it is hard to reconcile with the data from the 0.75- to 2.25-Hz band. How can we obtain nearly the same major axis skews in the borehole data when they are located well below the weathered layer? One explanation is that although at the lowest frequencies the boreholes are only a fraction of a wavelength below the surface, at the highest frequency observed here (21 Hz), the deepest borehole is only about 1 wavelength below the surface. Hence, it is conceivable that the borehole data are impacted by anisotropic properties of the near surface even though these sensors are located well below the weathered layer. This cannot be addressed, however, without more extensive modeling with synthetic seismograms that can properly model anisotropic media at finite wavelengths. This is beyond the scope of this article.

The next level of heterogeneity is structure at the scale of a geologic map. A rock unit called the Santa Rosa mylonite wraps around Piñon Flat (Fig. 2). Parcel (1981) argues the Santa Rosa mylonite was formed by right-lateral, horizontal transport and that the bend in this rock unit at Piñon Flat was induced by a deflection of the shear zone caused by interaction with the plutonic body that floors Piñon Flat. The Santa Rosa mylonite is a very strongly anisotropic rock. Kern and Wenk (1990) found these rocks to be transversely isotropic with a 5 to 19% anisotropy at surface pressures decreasing to 5 to 12% anisotropy at 600 MPa. Unfortunately, the sense of the anisotropy is the opposite of that determined from our inversion of these data. That is, the model we determined is a transversely isotropic medium dipping to the northwest with the fast axis perpendicular to the plane of symmetry. If we had pure Santa Rosa mylonite with its foliation plane dipping in the same northwesterly direction, the normal to the foliation plane would be in the slow axis, not the fast axis. What this means remains ambiguous because the subsurface geometry of the Santa Rosa mylonite beneath Piñon Flats is not known. Dibblee's (1981) maps (see Fig. 2) show the mylonites wrapping around the west and south side of Piñon Flats. Measured foliations dip eastward swinging to the north with angles ranging from 30 to 60°, suggesting the mylonites wrap around and underneath the granodiorite from both the south and west sides. How this complex geometry would map into our data is not at all clear.

The overall conclusion we reach is that the total effect we observe is probably the superposition of at least three processes: (1) near-surface anisotropy introduced by preferential weathering along joints in the granites, (2) a larger scale fabric induced by the Santa Rosa mylonite, and (3) near-surface scattering. The last process is probably most important in the highest frequency band (7 to 21 Hz) and probably contributes to the exceptionally large major axis skews seen from azimuths near 240°. There are several fundamental ambiguities that prevent us from fully sorting this

out with available data. First, we have only a loose idea of the subsurface geometry of the Santa Rosa mylonite. The best guess of the actual geometry (Fig. 2) is that the mylonite wraps around the area where these data were collected. We know of no existing program capable of modeling such a complex medium even if we had better constraints on its geometry. Second, our concepts of the interactions of the wave field with the near surface at this site are largely conjecture. The near-surface material at this site has heterogeneity on a wide range of scales from at least 0.001 to 100 m. We have considered attempting to model the near-surface material, but this is fraught with ambiguity for two reasons: (1) limited knowledge of subsurface structure and (2) fundamental questions about the validity of existing computer codes to properly model such a wildly heterogeneous medium.

The phenomenon we observe here is only observable with a three-component array. A question this article leaves hanging is: How common is this type of departure from the standard model of wave propagation in a layered Earth? We suggest that the methodologies developed here, when applied to three-component array data, can provide fundamental new observations on anisotropy within the Earth. Broadband data from arrays of varying scale have the potential to provide a new way to measure crustal anisotropy through application of the techniques described in this article.

Acknowledgments

References

Aki, K. and P. G. Richards (1980). *Quantitative Seismology Theory and Methods,* Vol. 1, Freeman, San Francisco, 557 pp.

Al-Shukri, H., T. Owens, G. Pavlis, S. Roeker, F. Vernon, and G. Wagner (1992). Data report for the 1991 Piñon Flat broadband array experiment, IRIS/*PASSCAL Data Report.*

Anderson, P. N. (1993). Animated visualization techniques for three-component seismic array data, *Ph.D. Thesis,* Indiana University.

Backus, G. E. (1962). Long-wave elastic anisotropy produced by horizontal layering, *J. Geophys. Res.* **67,** 4427–4440.

Bear, L. K. and G. L. Pavlis (1997a). Estimation of slowness vectors and their uncertainties using multi-wavelet seismic array processing, *Bull. Seism. Soc. Am.* **87,** 755–769.

Bear, L. K. and G. L. Pavlis (1997b). High-resolution multiwavelet seismic array processing, *EOS* **78,** S216.

Bear, L. K. and G. L. Pavlis (1999). Multi-channel estimation of time residuals from broadband seismic data using multi-wavelets, *Bull. Seism. Soc. Am.* **89,** 681–692.

Bokelmann, G. H. R. (1995a). P-wave array polarization analysis and effective anisotropy of the brittle crust, *Geophys. J. Int.* **120,** 145–162.

Bokelmann, G. H. R. (1995b). Azimuth and slowness deviations from the GERESS regional array, *Bull. Seism. Soc. Am.* **85,** 1456–1463.

Bokelmann, G. H. R. (1996). Local effects on P-wave polarization, in "Seis-

mic Anisotropy,* E. Fjaer, R. M. Holt, and J. S. Rathore (Editors), Society of Exploration Geophysicists, 763 pp.

Chave, A. D., D. J. Thomson, and M. E. Ander (1987). On the robust estimation of power spectra, coherences, and transfer functions, *J. Geophys. Res.* **92,** 633–648.

Dibblee, T. W. (1981). Geology of the San Jacinto Mountains and adjacent areas, in *Geology of the San Jacinto Mountains: Annual Field Trip Guidebook No. 9,* A. R. Brown and R. W. Ruff (Editors), South Coast Geological Society, Santa Rosa, California, 1–47.

Fletcher, J. B., T. Fumal, H. Liu, and L. C. Carroll (1990). Near-surface velocities and attenuation at two boreholes near Anza, California, from logging data, *Bull. Seism. Soc. Am.* **80,** 807–831.

Harvey, D. (1994). *dbap (a public domain computer program),* Joint Seismic Program Center, University of Colorado, Boulder.

Helbig, K. (1994). *Foundations of Anisotropy for Exploration Seismics,* Oxford, New York, 486 pp.

Husebye, E. S. and B. O. Ruud (1989). Array seismology; past, present, and future developments, in *Observatory Seismology,* J. J. Litehiser (Editor), University of California Press, Berkeley, 123–153.

Kern, H. and H.-R. Wenk (1990). Fabric related anisotropy and shear wave splitting in rocks from the Santa Rosa mylonite zone, California, *J. Geophys. Res.* **95,** 11213–11223.

Kvaerna, T. and D. J. Doornbos (1986). An integrated approach to slowness analysis with arrays and three-component stations, *NORSAR 2-85/86.*

Lilly, J. M. and J. Park (1995). Multiwavelet spectral and polarization analyses of seismic records, *Geophys. J. Int.* **122,** 1001–1021.

Lin, C. H. and S. W. Roecker (1996). P-wave backazimuth anomalies observed by a small-aperture seismic array at Piñon Flat, southern California: implications for structure and source location, *Bull. Seism. Soc. Am.* **86,** 470–476.

Ollier, C. (1969). *Weathering,* Elsevier, New York.

Owens, T., P. N. Anderson, and D. E. McNamara (1991). Data report for the 1990 Piñon Flat grid experiment: an IRIS Eurasian Studies Program passive source experiment, IRIS/PASSCAL Data Report #91-002.

Parcel, R. F. (1981). Structure and petrology of the Santa Rosa shear zone in the Pinyon Flat area Riverside County, California, in *Geology of the San Jacinto Mountains: Annual Field Trip Guidebook No. 9,* A. R. Brown and R. W. Ruff (Editors), South Coast Geological Society, Santa Rosa, California, 139–150.

Pavlis, G. L. and H. Mahdi (1996). Surface wave propagation in central Asia: observations of scattering and multipathing with the Kyrgyzstan broadband array, *J. Geophys. Res.* **101,** 8437–8455.

Peacock, S., S. Crampin, D. C. Booth, J. B. Fletcher (1988). Shear wave splitting in the Anza seismic gap, southern California: temporal variations as possible precursors, *J. Geophys. Res.* **93,** 3339–3356.

Vernon, F. L., J. Fletcher, L. Carroll, A. Chave, and E. Sambera (1991). Coherence of seismic body waves from local events as measured by a small-aperture array, *J. Geophys. Res.* **96,** 11981–11996.

Vernon, F. L., G. L. Pavlis, T. J. Owens, D. E. McNamara, and P. E. Anderson (1998). Near-surface scattering effects observed with a high-frequency array at Pinyon Flats, California, *Bull. Seism. Soc. Am.* **88,** 1548–1560.

Vidale, J. E. (1986). Complex polarization analysis of particle motion, *Bull. Seism. Soc. Am.* **76,** 1393–1405.

Wagner, G. S. (1994). Analysis of multidimensional JSP data, IRIS *Newslett.* (summer), 13–16.

Wagner, G. S. (1997). Local wave propagation in the San Jacinto Fault Zone, southern California: observations from a three-component seismic array, *J. Geophys. Res.* **102,** 8285–8311.

Wagner, G. S. and T. J. Owens (1993). Broadband bearing-time records of three-component seismic array data and their application to the study of local earthquake coda, *Geophys. Res. Lett.* **20,** 1823–1826.

Wagner, G. S. and T. J. Owens (1995). Broadband eigen-analysis for three-component seismic array data, *IEEE Trans. Signal Process.* **43,** 1738–1741.

Wagner, G. S. and T. J. Owens (1996). Signal detection using multi-channel seismic data, *Bull. Seism. Soc. Am.* **86**, 221–231.

Werner, U. and S. A. Shapiro (1998). Intrinsic anisotropy and thin multi-layering—two anisotropy effects combined, *Geophys. J. Int.* **132**, 363–373.

Wilson, D. C. (1997). Near-surface site effects in crystalline bedrock: azimuthal dependence, scale lengths of spectral variation, and change in spectral character with depth, *Master's Thesis*, Indiana University, 27 pp.

Wilson, D. C. and G. L. Pavlis (1999). Near-surface site effects in crystalline bedrock: a comprehensive analysis of spectral amplitudes determined from a dense, three-component seismic array, *Earth Interactions*, in press.

Wyatt, F. (1982). Displacement of surface monuments: horizontal motion, *J. Geophys. Res.* **87**, 979–989.

Department of Geological Sciences
Indiana University
1001 East 10th Street
Bloomington, Indiana 47405
   (L. K. B., G. L. P.)

Institute of Geophysics
Ruhr-University Bochum
D-44780 Bochum, Germany
   (G. H. R. B.)